ASME Journal of Turbomachinery
Online journal at:
https://asmedigitalcollection.asme.org/turbomachinery

Edwin J. Munoz Lopez[1]
Institute of Propulsion Technology,
German Aerospace Center (DLR),
Linder Höhe, Cologne 51147, Germany
e-mail: edwin.munozlopez@dlr.de

Alexander Hergt
Institute of Propulsion Technology,
German Aerospace Center (DLR),
Linder Höhe, Cologne 51147, Germany
e-mail: alexander.hergt@dlr.de

Joachim Klinner
Institute of Propulsion Technology,
German Aerospace Center (DLR),
Linder Höhe, Cologne 51147, Germany
e-mail: joachim.klinner@dlr.de

Bjoern Klose
Institute of Test and Simulation for Gas Turbines,
German Aerospace Center (DLR),
Linder Höhe, Cologne 51147, Germany
e-mail: bjoern.klose@dlr.de

Chris Willert
Institute of Propulsion Technology,
German Aerospace Center (DLR),
Linder Höhe, Cologne 51147, Germany
e-mail: chris.willert@dlr.de

Volker Gümmer
Chair of Turbomachinery and Flight Propulsion,
Technical University of Munich (TUM),
Boltzmannstraße 15, Garching 85748, Germany
e-mail: volker.guemmer@tum.de

The Unsteady Shock-Boundary Layer Interaction in a Compressor Cascade—Part III: Mechanisms of Shock Oscillation

The shock-boundary layer interaction in transonic flows is known to cause strong unsteady flow effects that negatively affect the performance and operability of blade and cascade designs. Despite decades of research on the subject, little is still known about the physical mechanisms that drive the different oscillation frequencies observed with different designs. In the conclusion of this three-part series, the experimental and numerical data obtained with the Transonic Cascade TEAMAero are analyzed together in detail in order to test the main theories of continuous shock oscillation. This analysis exposes a main mechanism of shock oscillation, where pressure waves generated inside the passage of the cascade propagate upstream and interact strongly with the main shock when the latter is also in the passage. The interaction of these features causes a breakdown of the flow that is shown to propagate upstream, inevitably causing strong variations in the inflow angle and therefore on the operating conditions of the cascade. The high-frequency content of these pressure waves is also shown to be responsible for weaker high-frequency variations of the shock movement throughout the cycle. Parallels are also drawn with previous experimental campaigns in order to search for a global understanding of the different observations made. Although various parts of the described interaction are not fully understood yet, and the dataset of experimental measurements compiled is still rather small, a good basis is provided on which to further study the underlying mechanisms of unsteady flows in transonic cascades. [DOI: 10.1115/1.4066186]

Keywords: compressors, SBLI, unsteady, experimental, PIV, CFD, LES

1 Introduction

The flow through a transonic compressor blade row is highly and naturally unsteady. This behavior is known to cause several detrimental effects on the performance and reliability of compressor machines [1,2]. However, it is also a feature that is common among supersonic flows due to the ubiquitous presence of complex shock-boundary layer interactions (SBLI), documented as early as the 1940s [3,4]. The detailed study of these interactions has led to evidence that points to very different hypotheses attempting to explain the nature of the sustained oscillations in different applications [5–8]. Some of these explanations point to mechanisms of propagation of disturbances in different directions: downstream from the incoming flow, and upstream from the flow interactions downstream of the shock [9]. Other explanations focus on the interaction of the shock with its own separation bubble at the shock foot [10].

The most common explanation for continuous shock oscillation in applications of aerodynamic profiles seems to be the trailing edge feedback mechanism originally proposed by Lee for supercritical airfoils [6,11]. This mechanism relates the shock motion to the interaction between turbulent structures that propagate downstream of the shock with the trailing edge of the geometry. The interaction of these vortical structures would then result in pressure waves that propagate upstream in a continuous, self-sustaining manner. Evidence of said mechanism has been found in both experimental [12] and numerical studies of different fidelity levels [7,13].

Within the context of axial compressor flows, Priebe also shows in Ref. [14] evidence of the same type of trailing edge feedback with high-fidelity simulations at different operating conditions of a compressor cascade. Similar conclusions were also obtained with lower fidelity numerical methods in Ref. [15], where a full-annulus domain with an unsteady Reynolds-averaged Navier–Stokes (URANS) solver is shown to capture the propagation of said disturbances from the trailing edge in both axial and circumferential

[1]Corresponding author.

Contributed by the International Gas Turbine Institute (IGTI) of ASME for publication in the Journal of Turbomachinery. Manuscript received July 11, 2024; final manuscript received July 24, 2024; published online February 7, 2025. Tech. Editor: David G. Bogard.

directions. However, the flow through a row of compressor blades is highly complex due to the physical constraints imposed by the geometry and the interactions that occur between itself, the (ideally) periodic shock structure, the turbulent flow after the shock, and the inevitably instationary flow conditions at the outlet of the blade row. These factors provide many possible sources of unsteadiness, so that a deeper understanding of the mechanisms at play is required to be able to model, predict, and mitigate such behavior in future designs.

The DLR has continuously contributed to this research effort experimentally by applying advanced measurement techniques on different transonic compressor cascades at the Transonic Cascade Wind Tunnel (TGK) in Cologne, a unique facility in operation at the DLR since the 1970s [16,17]. More recently, using high-speed Schlieren (HSS) to capture the flow over the TFAST cascade, it was shown that tripping a laminar boundary layer to turbulent before the shock suppressed the high-frequency tones previously present in the spectra of the shock oscillation [1]. With the LHT cascade, it was observed instead that these high-frequency tones were amplified when the cascade operated near stall. Applying high-speed particle image velocimetry (PIV) on this cascade, it was also observed that disturbances on the flow velocity components propagated from a point downstream of the shock, but upstream of the trailing edge [18,19]. This contrasts then clearly with Lee's theory of trailing edge feedback.

The latest work packages focus on the Transonic Cascade TEAMAero (TCTA). For this cascade, three passages were first measured simultaneously with HSS to reveal interactions between adjacent passages and a broad main frequency band of oscillation between 500 and 550 Hz, modulated again by a strong high-frequency tone at 1140 Hz [20]. A further study on this cascade with high-resolution PIV and proper orthogonal decomposition analyses showed the different spatial modes of oscillation of the flow in the passage [21]. At the same time, the DLR has made considerable improvements to its CFD solver for turbomachinery applications, TRACE, in order to perform efficient high-fidelity large eddy simulation (LES) of cascade configurations to compare with experiments [22–24]. This solver has already provided new insights into the flow of the LHT cascade, although it was determined that longer simulation times are required to allow a better comparison with the experimental data [25,26].

This article is then not only the culmination of this three-part contribution, over which the experimental and numerical results have been presented separately in detail, but also the culmination of a multi-year effort to bridge the gap between experiments and numerics. This was necessary in order to achieve the best possible understanding of the unsteady SBLI flow through the TCTA. For this purpose, a new experimental campaign was performed with this cascade using HSS and high-speed PIV (HSPIV) techniques at different regions of interest. In addition to this, high-fidelity LES simulations were performed of the same configuration and operating conditions, albeit with a smaller periodic domain in both pitch and blade span. The main unique feature of this simulation lies in the long simulation time computed, over 100 convective time units (t_c). The extensive amount of numerical data gathered allows a relevant and accurate comparison with the experimental results. The following sections present the design of the TCTA used for this study, describe the experimental and numerical methods employed, discuss the results in detail, and summarize the conclusions drawn from this interdisciplinary effort.

2 The Transonic Cascade TEAMAero

The TCTA is a transonic compressor cascade designed by means of multi-objective optimization with the DLR's in-house numerical software including the optimization suite, AutoOpti, and the CFD solver, TRACE. The latter was configured with the RANS k–ω turbulence and γ–Reθ transition models to solve the flow through the different design candidates. A detailed recount of the numerical validation and optimization process can be found in Ref. [27], while

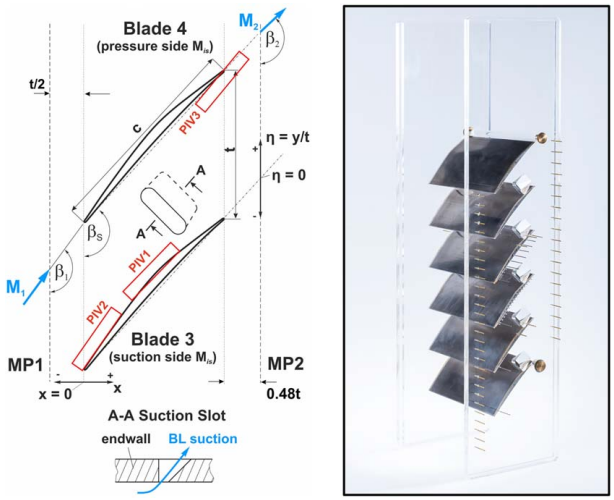

Fig. 1 The Transonic Cascade TEAMAero: design definition (left) and manufactured assembly (right)

Table 1 Cascade design properties and operating conditions

	TCTA	LHT	TFAST
Blade chord, c (mm)	100	70	100
Pitch, t (mm)	65	49.5	60
Stagger angle, β_{st} (deg)	135.8	139.9	134.4
Inflow angle, β_1 (deg)	145.7	151.3	145.5
Inflow Mach, M_1	1.21	1.05	1.21
Outflow Mach, M_2	0.64	0.57	0.77
de Haller number, DH	0.582	0.577	0.683
Temperature, T_1 (K)	235.9	245.0	235.4
Reynolds number (10^6)	1.35	1.13	1.38
Axial velocity density ratio	1.05	1.00	1.21
δ_{99} at $x/c = 0.3$ (mm)	0.444	0.34	–
Mean shock position, $\bar{x}_s/c$	0.526	0.390	0.519
Appr. vel. pre-shock, $\overline{V}_{s_1}$ (m/s)	395	375	400
Appr. vel. post-shock, $\overline{V}_{s_2}$ (m/s)	280	255	300

the final design definition and the assembly manufactured for the TGK facility are shown in Fig. 1. The main properties of this design are summarized in Table 1, along with those of the similar cascade designs discussed in the previous section, which will become relevant in later sections. The operating conditions reported are measured at the measurement plane (MP) 1, as shown in Fig. 1. Finally, the performance and working range of the final TCTA design were validated experimentally with steady measurement techniques [28].

However, the main purpose of the new design is to study the unsteady SBLI that occurs within the passages of the cascade. This line of work was started via HSS measurements of the shock movement in the three adjacent middle passages at the cascade's aerodynamic design point (ADP) [20]. This work package revealed that this movement is rather similar across the passages, with a broad main frequency band of oscillation between 500 and 550 Hz that is modulated with a strong frequency tone at 1140 Hz. The passages were also revealed to have a certain level of interaction with each other. For instance, the shock movement in the second and third passages correlated strongly with each other at a lag that approximately corresponds to the distance between their bow shocks and the mean flow velocity.

Further analyses were performed on this cascade via 2D-2 component and high-resolution PIV measurements of the flow in the middle passage of the cascade [21]. These measurements allowed the modal analysis of the velocity components, revealing a main mode of oscillation similar to a "bubble breathing" mode. This is due to the highly instationary nature of the size of the laminar

separation bubble under the shock throughout the cycle. The wall-normal velocity modes also show evidence of oscillation due to lambda-type structures that form in front of the shock. Although these results could not link the modes of oscillations with the different frequencies reported, they served as a starting point and inspiration for the continued analysis of the flow in this cascade. This time, however, with time-resolved measurements and analyses that take into account this time coherence, such as the spectral proper orthogonal decomposition (SPOD).

Some of the main questions that remain to be resolved are the following: What is the origin of the different frequencies of oscillation observed in the shock spectra? What factors are responsible for the specific frequency bands and tones measured in different operating conditions? And what aerodynamic mechanisms can possibly allow these different types of oscillations? The focus of the current work package is then to bring together time-resolved experimental and numerical methods in order to obtain a more complete picture of the flow inside this cascade and start addressing these questions.

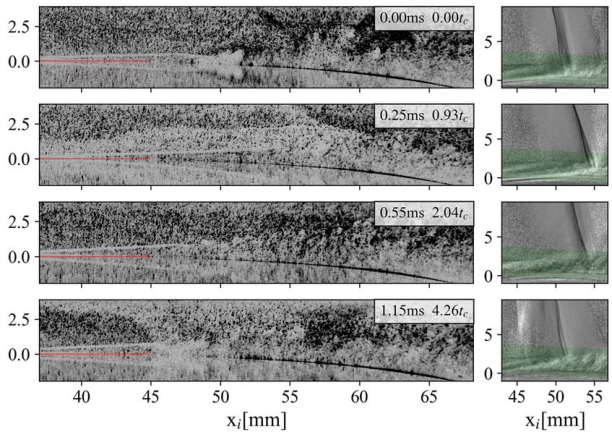

Fig. 2 Cross-correlated sequence of HSPIV images (left) and shadowgraphs (right) of the flow near the blade during forward shock movement. Blade surface is indicated with a red line.

3 Experimental Methods

The main experimental results considered for this comparison stem from the HSPIV measurements performed and described in detail in Part I of this submission. For the full description of the methods applied for the acquisition of these data, the reader is referred to said article, although a brief recount of the most important aspects is given here for completion. As previously discussed, shock movement in the TCTA occurs at frequencies in the order of 10^2 to 10^3 Hz. The HSPIV acquisition rate was then configured to 40–46 kHz, corresponding to sampling frequencies of the flow of 20–23 kHz. This was done with a high-speed camera (Phantom v2640) equipped with a macro lens (Nikon, Nikkor Micro f200/4) at a magnification of 19.6 μm/pixel.

Due to the high frame acquisition rates required, the camera is set to image sizes of 1792×200 pixels for the highest sampling of 23 kHz, and 1792×328 pixels for the lowest one at 20 kHz. Particle illumination is provided by a high-repetition double-pulse laser system providing up to 10 W of power at pulse separations between 1 and 1.2 μs. This provides sufficient particle image intensity for a light sheet height of 4 mm and thickness of 0.2 mm. The regions of interest sampled with HSPIV are shown in red in Fig. 1. These regions capture the flow over the suction surface near the leading edge and under the shock foot, and along the pressure side of the adjacent blade near the trailing edge.

Given that the light sheet is small, an ideally synchronous recording with a second Phantom v1840 camera is performed to reliably capture the position of the shock with shadowgraph images of a wider field of view in the cascade passage. This camera is equipped with a Nikkor Micro 200/5.6 lens and configured to an image size of 511×511 pixels with a magnification of 45 μm/pixel. The region captured with the HSS setup is illuminated by a high-power red light-emitting diode (LED), providing short duration pulses for the desired frame rates. Since the cameras are capturing overlapping areas, the image capturing paths of the laser pulses and LED are separated via a dichroic mirror.

These cameras are setup as master and slave in order to synchronize their operation. However, issues with the trigger mechanism prevented the cameras from obtaining the synchronous images intended. Instead, the images lag each other by about 2 s and correspond to non-overlapping time windows. Nevertheless, the analyses performed in this paper with the different sets of data stand well on their own. Additionally, cross-correlations of the shock movement from the different recordings help align some sequences of similar shock movement for visualization as it was originally intended, as shown in Fig. 2.

To process these recordings, the movement of the blade is also estimated based on a correlation algorithm using the intensity distribution in each sample region with several template images of reference blade positions. Further pre-processing is performed with the images in order to enhance the particle image contrasts to allow validation rates of at least 95% per burst at interrogation windows of 64×16 pixels. Higher validation rates are possible with larger window sizes, but the narrower one is preferred to enhance visibility of the structures in the separation bubble and reduce window overlap with the blade edge.

4 Numerical Methods

The numerical methods have also been described in detail in Part II of this series. However, they are briefly presented here as well for completion. The simulation results that are presented in this paper were calculated with TRACE's discontinuous Galerkin spectral element method solver. An extensive and detailed implementation of the method is found in Refs. [22–24].

The flow over the TCTA cascade is simulated at the ADP operating condition with $M_1 = 1.21$, $\mathrm{Re}_1 = 1.35 \times 10^6$, and $\beta_1 = 145.7$ deg, measured at the MP1 as in the experiments. For this LES simulation, an implicit (no-model) approach is chosen for the modeling of subgrid stresses, such that dissipation is added implicitly via the numerical dissipation of the Riemann solver. Furthermore, the entropy-conserving split-form variant is applied together with the corresponding Riemann solver to cancel numerical errors arising from the non-linearity of the advective fluxes. Spurious oscillations across shock fronts in the high-order accurate LES are avoided by applying a finite volume subcell shock capturing method. A feature-based dilatation-vorticity sensor is used to identify the elements that require such blending.

The domain consists of inlet and outlet boundaries located 1.0 chord length upstream and 1.5 chord lengths downstream of the leading and trailing edges, respectively. The inflow and outflow boundary conditions used are the 1D non-reflecting boundary conditions from Ref. [29], with the total pressure, total temperature, and flow angle specified at the inlet and static pressure at the outlet. Periodic boundary conditions are set along the spanwise and pitchwise directions. The computational grid itself is generated with the Gmsh package and contains 108,564 hexahedral elements in the x- - y plane with a structured refinement around the shock location to avoid spurious flow structures. The mesh is extruded by 10% chord length along the spanwise direction and a polynomial order of $N = 3$ is used in all elements, yielding a fourth order accurate spatial discretization. The equations are advanced in time with an explicit third-order Runge–Kutta scheme.

Excluding the leading and trailing edges, the maximum non-dimensional cell sizes are $\Delta\xi^+_{\max} = 35$, $\Delta\eta^+_{\max} = 2$, and $\Delta\zeta^+_{\max} = 25$. The values are normalized by the polynomial order N to aid the comparability to finite volume simulations, and they are comparable to other high-Reynolds number compressor studies [24,30]. This was the most refined grid studied with a

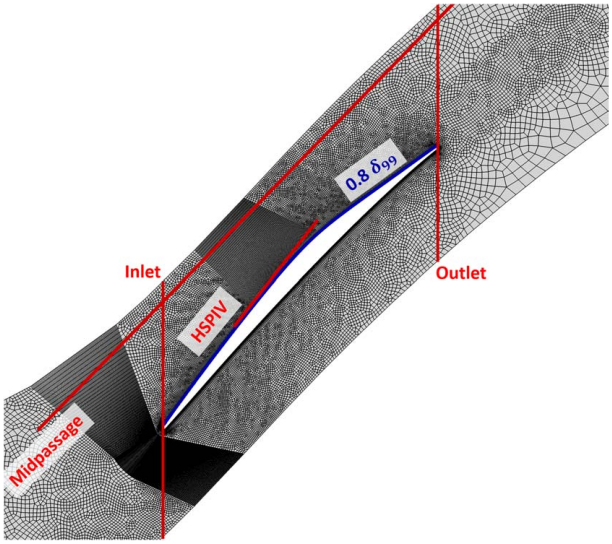

Fig. 3 Coarse computational grid of the TCTA showing only elements without interior nodes. Some probe lines sampled in the domain are marked.

span size that seemed to be wide enough to avoid with some margin the non-isotropic turbulence at the midspan of the cascade originating from the periodic boundary conditions. The span of 10% of the chord length with this domain corresponds to 6% of the cascade span as installed in the TGK. The entire domain was sampled throughout the simulation with a coarser regular grid and multiple 1D line probes. A coarse version of the domain and the mesh is shown in Fig. 3, along with some of the relevant probe lines sampled.

5 Results and Discussion

From the experiments, there were a total of 14 measurement runs with 8 bursts, each of them capturing over 10,000 shadowgraphs and 20,000 PIV images. With a sample frequency between 20 and 23 kHz for the different runs, this amounts to more than 56 s of footage in the different regions of interest. The LES results, on the other hand, have been sampled in detail with a number of 1D, 2D, and 3D probes over different parts of the domain. However, despite the long simulation time computed, they still consist of "only" about 30 ms of footage. A meaningful analysis of all the data then requires careful consideration to draw on the strengths of each dataset.

The first results presented in Fig. 4 are the frequency-weighted power spectral densities (PSD) of the shock motion for both

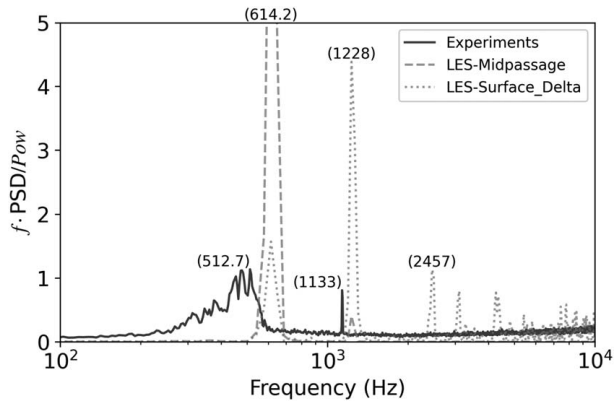

Fig. 4 PSD of the shock movement in the passage of the TCTA from experiments and LES

datasets. The spectrum of the experiments is the average of all the recordings made. It peaks broadly over a 50 Hz band around 500 Hz and then narrowly at a tone of 1133 Hz, similar to previous experimental campaigns. The LES on the other hand shows a more tonal spectrum, starting with the main frequency of the shock at 614 Hz and repeating over its harmonics. Two lines are shown for the LES, one spectrum is obtained from a "perfect" tracking of the shock position at the blade midspan using a midpassage probe line and applying a modified Ducros sensor as in Ref. [30]. The second one is obtained with an imperfect tracking of the shock via a density gradient sensor and a probe line closer to the blade surface. The latter is meant to imitate the type of shock tracking allowed by the integrated shadowgraph images. This signal is more noisy with a broader peak for the main shock movement and a strongly highlighted tone at 1228 Hz.

This simple comparison helps guide the remaining analyses. This paper is indeed *not* trying to prove that the LES and experimental results are one and the same. They require different interpretations due to their inherent differences. The flow in the LES simulations with perfectly periodic domain is rather two-dimensional. Regardless of the span validation study in Part II, the shock front is observed to move uniformly across the span. On the other hand, the flow in the experiments is three-dimensional in nature. It is affected by the suction slots in the passage, the aperiodicity from the inevitable shock reflections in the test section, and by the vibrations of the blade itself that occur near 400 Hz and were discussed in Part I. These key differences alone may explain the shift of the frequency peaks of nearly 100 Hz, or the increased amplitude of the oscillation by about 10% of the chord length in the LES. And yet, in spite of these differences, the results are remarkably close to each other. What this paper is then actually trying to prove is that these results exhibit the same mechanism of shock oscillation, which will be elucidated in the following sections.

The remaining sections start by presenting one full cycle of oscillation by leaning on the detail of the LES results. A thorough comparison with the experimental measurements is then performed in order to establish the validity of the LES results with respect to the experiments. Further analyses are then shown to narrow down and present the perceived mechanism of oscillation of the TCTA. The final section brings these results together with those of previous experimental campaigns to investigate the transferability of this new knowledge to other configurations.

5.1 The Shock Oscillation Cycle of the TCTA. The main cycle of oscillation in the LES results occurs at a frequency of 615 Hz, as shown in Fig. 4. In order to visualize this cycle, the mean pressure and Mach number fields of the flow are first presented in Fig. 5, along with four equi-temporal snapshots of this cycle in Fig. 6. The latter show the Mach number and the pressure variation with respect to the mean field previously shown ($P' = P - \bar{P}$). A more detailed sequence of this cycle is also presented in Part II of this series.

In Fig. 6, the shock starts at its most upstream position. One of the main features of the flow is already identified, which is the presence of an oblique shock propagating upstream from the main shock. These oblique shocks are periodically observed in the flow throughout the simulation. They create not only a visible slip line and a variation of the shock strength across the passage, but they also inevitably increase the incidence of the incoming flow. Another important feature identified is the downstream convection of a block of recirculating flow from the previous cycle. The interaction of this separated flow with the trailing edge has already produced two strong vortices. More importantly, its previous interaction with the flow in the passage seems to have generated a pressure wave that is propagating upstream. This shocklet-type feature may well have been generated by the blockage caused by the downstream propagation of the separated flow, which is an uneven and transient effect by nature.

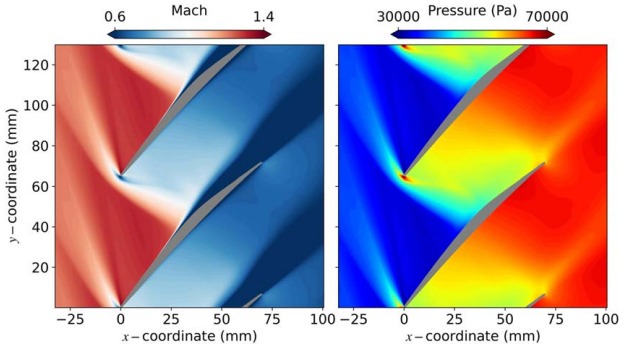

Fig. 5 Mean Mach number and pressure fields of the TCTA through the simulation

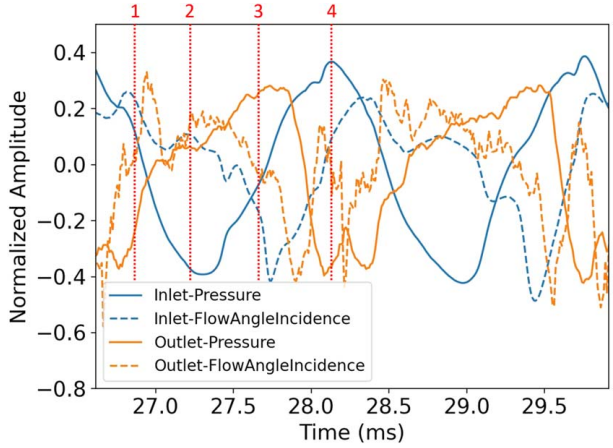

Fig. 7 Averaged quantities at the inlet and outlet of the cascade over one cycle of oscillation

Moving on to the second frame, the number of shocklets has increased in the wake of the downstream convection of the separated flow. The main shock on the other hand is now moving into the passage, and it already seems to interact with one of the shocklets. The latter are then clearly moving at a faster speed than the main shock. The separation in the passage is at a minimum, and the vortex shedding at the trailing edge is decreasing. Note that even though the shock is moving into the passage, that is, its topology is becoming more oblique and the incidence of the incoming flow is therefore decreasing, the pressure at the outlet of the cascade seems to be increasing instead. The shocklets themselves also seem to be transmitting this increased pressure, albeit somewhat unevenly along the passage.

In the third frame, the shocklets have already coalesced and interacted strongly with the main shock. The separated flow at the trailing edge is at a minimum and the vortex shedding has completely stopped. However, the separation bubble under the shock has grown considerably due to the strong oblique shock propagating upstream at high speed. This oblique shock causes the pressure and incidence of the flow to rapidly increase again. The increased bubble size itself causes a series of secondary shocks in the passage. The cascade seems to choke momentarily, increasing the pressure behind the shock and causing the flow under the shock foot to break down. In the final snapshot, the breakdown has occurred and a block of separated flow convects downstream. The main shock is again normal and already almost where it started, that is, the upstream movement occurs remarkably faster than the rest of the cycle. The vortex shedding has already restarted, which seems to be a key factor for the decreased pressure at the cascade outlet that sets up the next cycle.

The dynamic between the inlet and the outlet of the cascade is particularly interesting throughout the cycle. This given that the back-pressure is shown to be low when the shock is at its most upstream position and high when the shock is in the passage, when the opposite is expected. This can be observed in Fig. 7, where the pressure and the flow incidence were averaged and Favre-averaged, respectively, over two cycles of oscillation. The cycle shown in Fig. 6 is marked accordingly with red dotted lines. Note that cascade inlet and outlet refers to the lines joining the leading and trailing edges of adjacent blades in Fig. 3, and that the signals have been normalized with their maximum amplitudes. The pressure signals are shown to oscillate at opposite phase with each other. The highest outlet pressure also seems to coincide with the lowest flow incidence, contrary to

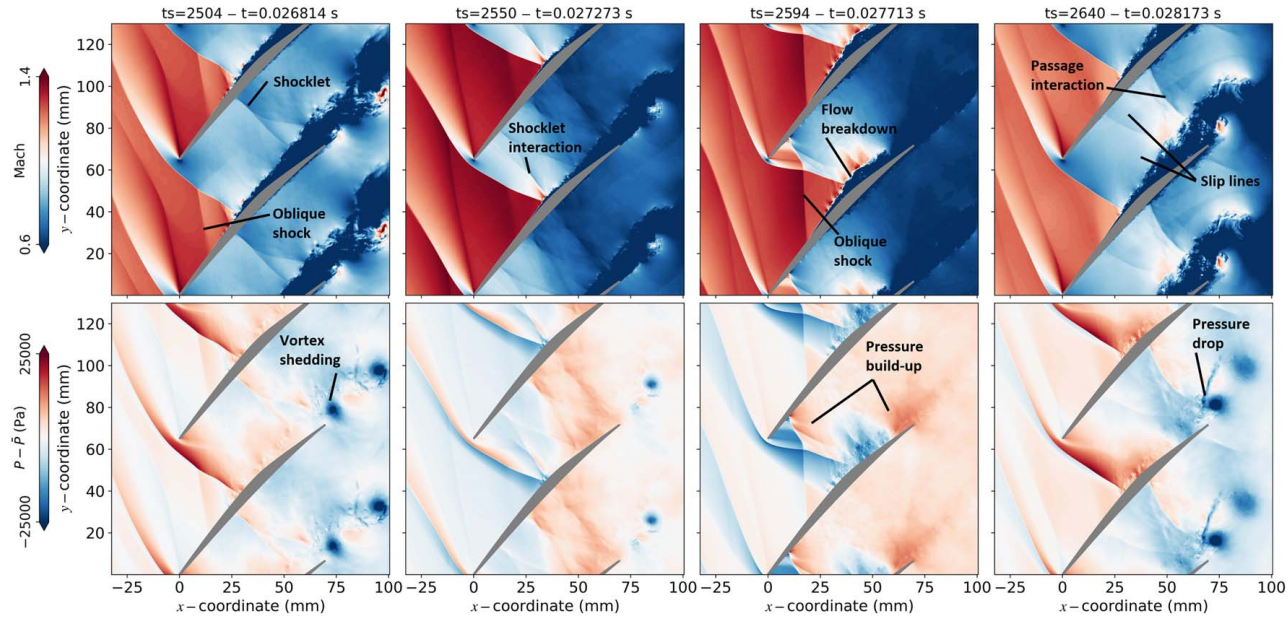

Fig. 6 Mach and pressure variation contours of one cycle of shock oscillation observed in the high-fidelity simulations of the Transonic Cascade TEAMAero

what would be expected if two stationary operating points were being analyzed.

A simple correlation of these signals (not shown) confirms also that the maximum correlation peak is found at 0.567 ms and subsequent peaks are found with a frequency of 627 Hz. This means that on average, the signal at the outlet is indeed following the inlet with an average equivalent speed of propagation of about 176 m/s. This already hints to at least two different mechanisms that might be at play in this cycle: one responsible for the generation and upstream propagation of the shocklets and oblique shocks at higher frequencies, and another downstream mechanism at lower frequencies that seems unable to negotiate the conditions between the inlet and the outlet.

These mechanisms can be visualized with a space–time diagram of the density gradient vector projected on the blade chord axis from the midpassage probe, as shown in Fig. 8. In this figure, the main shock is tracked with a green line, while the red lines highlight the oblique shocks and shocklets in the passage. These shocklets seem to be generated after the flow breakdown occurs and even seem to shortly convect downstream with the separated flow before rapidly propagating upstream. These pressure waves cannot propagate directly past the main shock, but it seems that the pressure information is transmitted through the boundary layer periodically in the form of the oblique shocks. Sometimes this occurs with a lag across the main shock and sometimes almost without lag, as shown in the figure detail.

The oscillating red line near 20% is the lip shock, which seems to be at its most downstream position (lowest inflow angle) precisely when the strongest upstream propagating oblique shocks of the adjacent lower blade reach the leading edge of its upper neighbor. This movement then in turn seems to be linked with the movement of the bow shock, which is seen periodically at 0% chord. Note in this figure that the upstream propagation of the shocklets does not seem to start at a preferred location, for instance at the trailing edge. Instead, their upstream propagation seems to be linked to the complex interaction of the separated flow in the passage as it convects downstream. This upstream propagation then seems to start close to the trailing edge, but not necessarily there, many times before, but sometimes even after it.

In this section, we have now gathered some of the footprints left by the mechanisms of oscillation. However, further analysis is required in order to quantify these features and associate them to the frequencies observed in the oscillation spectra.

5.2 Validating High-Fidelity Simulations With Experiments. The cycle of oscillation described in the previous section is validated by both qualitative and quantitative means. We start by presenting a sequence of two cross-correlated HSS and HSPIV recordings that capture two separate, but very similar flow breakdown events, as shown in Fig. 9. In these sequences, the main shock moves deep inside the passage, and it seems to interact with the different shocklets moving upstream. As this interaction unfolds, the separation bubble under the shock foot grows considerably, the shocklets branch out or fade away, and a number of oblique shocks are shown to propagate upstream. The PIV frames show this same process occurring with a lot of similarities between the recordings, which can be expected to occur as the process is cyclical and recurrent in nature.

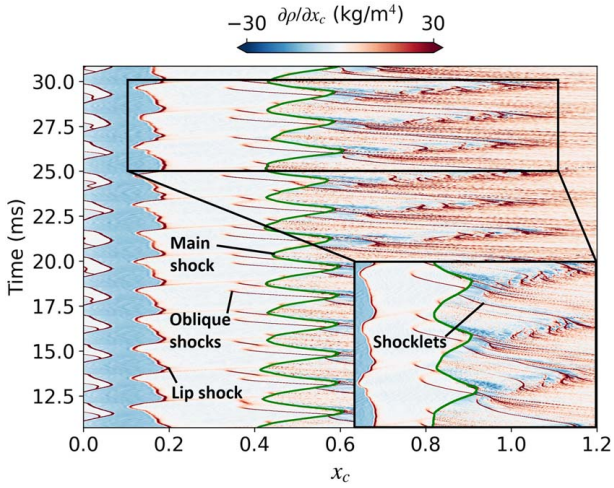

Fig. 8 Space–time diagram over the midpassage probe with contours of the density gradient vector projected on the chord axis of the TCTA

Just like in the LES then, the experiments show a significant interaction between the main shock and these recurring upstream moving shocklets. Their nature, however, makes them difficult to quantify into a continuous position signal, as is usually done with the main shock. This given that the strength and visibility of the shocklets are inconsistent, and the image is focused to primarily capture the main shock. Nevertheless, a manual analysis of eight discrete sequences where the shocklets were clearly visible allowed the tracking of their position over usually 4–8 different frames. The tracking was performed via the gradient of the image along pixel rows. The position signal can then be evaluated into a shock or shocklet velocity based on the movement of the shock along that pixel row and the magnification of the camera.

This analysis revealed that the shocklets are moving with speeds between 20 and 50 m/s. This is noticeably faster than the main shock, which is oscillating with speeds up to 10 m/s. A similar analysis was done with five sequences of the oblique shocks, this time more easily captured along the pixel rows of the HSPIV frames, and also revealed speeds of upstream propagation between 30 and 50 m/s. This is on par with what was observed and quantified in the LES results, where this analysis can be done more consistently than in the experiments.

Further quantitative comparisons are shown in Fig. 10. This figure compares the frequency-weighted PSD contours averaged from all the bursts of one experimental run (top) with those from the LES (bottom). On the left, a row of pixels from the middle of the shadowgraph images is analyzed for the experiments, while the density gradient magnitude from a similar line is used for the LES. The contours are normalized by the power of the signal at each location. On the right, the velocity magnitude signal is analyzed from a row of pixels near the suction surface from the HSPIV along with a similar probe line for the LES. In all plots, the min., max., and mean positions of the shock are marked in red dashed lines. The results at first glance seem considerably different due to the tonal nature of the oscillations in the LES and the more noisy signals from the experiments. In addition to this, the experiments are strongly marked downstream of the shock by the 1.13 kHz tone previously identified, and by its first harmonic near 2.2 kHz upstream of the shock. The LES, on the other hand, is more strongly marked at higher frequencies by the third harmonic near 1.8 kHz.

Nevertheless, the results do agree in some key details. With all plots, it can be observed that the higher frequencies are clearly present downstream of the shock, but they are reinforced upstream of the shock and the energy is shifted to even higher tones. In the density gradient PSDs, the presence of the higher tones must then refer to the shocklets and their propagation as oblique shocks upstream of the shock. The main shock frequency band is also clearly present downstream. As was previously observed, the shocklets do interact strongly with the main shock when it is at its most downstream position. These observations are supported by the velocity magnitude PSDs, where a similar energy shift to higher frequencies can also be observed. Finally, the region inside the shock is equally difficult to interpret throughout. The appearance and disappearance of different frequencies observed might be due to the fact that the shock is oscillating and also acts as the source and sink of the structures occurring at different frequencies. The contour in this area might also hint at non-linear interactions

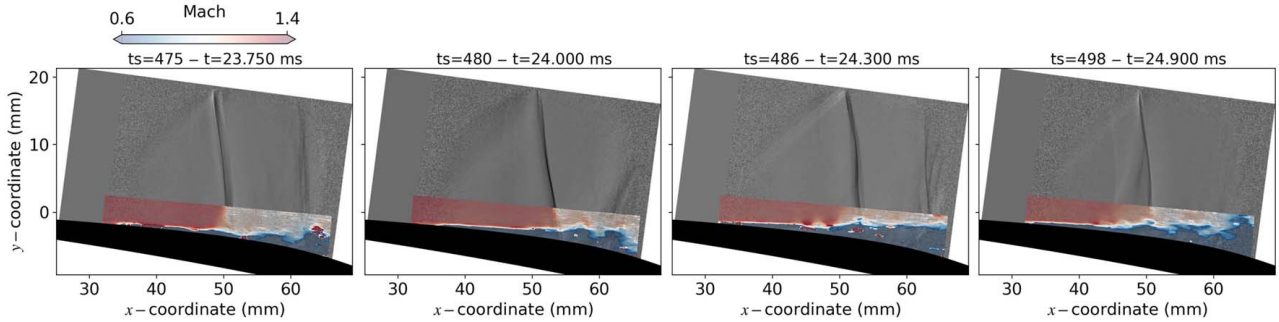

Fig. 9 Cross-correlated high-speed shadowgraph and PIV sequences of the shocklet interaction and flow breakdown in the passage of the TCTA

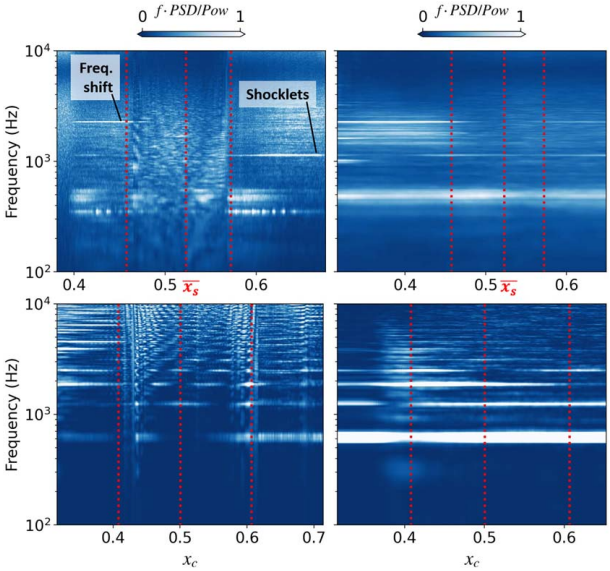

Fig. 10 Frequency-weighted power spectral densities from the experimental (top) and LES (bottom) results: left corresponds to shadowgraph image intensity (exp.) and density gradient (LES), right corresponds to the velocity magnitude (exp. and LES)

between these features, which could also explain the apparent shift to higher frequencies in both set of results.

Finally, a wave propagation analysis is shown in Fig. 11, where the two-point cross-correlation coefficient function ($R_{x'_0x'}$) is applied along pixel rows of the shadowgraph and a similar probe line in the LES, as defined below and also applied in Refs. [15,18]:

$$R_{x'_0x'}(\tau) = \frac{\sum_{t=0}^{k} x'_0(t)x'(t+\tau)}{\sigma_{x'_0}\sigma_{x'}} \tag{1}$$

where τ represents the lag between the zero-mean signals and σ is their standard deviation. The reference signal is arbitrary and is marked in the figure with a black dashed line. The signals are bypass filtered between the high-frequency bands of interest: 1100–1200 Hz for the experiments and 1700–1900 Hz for the LES. The figure shows that the slope of the correlation both in the experiments and in the LES is negative before and after the shock. This indicates an upstream flow of information that occurs at a speed determined by the slope of the linear squared fit of the correlation peaks, shown with a solid black line. The slopes measured indicate speeds of 28.3 m/s for the experiments and 26.2 m/s for the LES before and after the shock.

The region enclosed by the limits of the shock is again difficult to interpret. There is some evidence of both upstream and downstream propagation, and regions where the correlation contour is flat, which indicates simultaneous oscillation at the given frequency bands. It is worth noting here that a similar analysis of the density gradient filtered between 450 and 650 Hz (not shown) revealed mainly downstream propagation of information before and after the shock for experiments and LES. There are two types of analyses that could further clarify the interactions in the region of the main shock: PSD and cross-correlations in a frame of reference that follows the main shock, and non-linear spectral analyses, for instance with a bispectrum of relevant frequencies at the mean shock position. These analyses were not readily available, but this section has already shown that similar mechanisms of oscillation are occurring based on the evidence gathered.

5.3 Searching the Origin of the Shock Oscillation. In this section, the LES results are analyzed further in order to narrow down on the origin of the interactions and oscillations that were compared in the previous sections. For this purpose, cross-correlations are performed over different probe lines of interest. This part of the analysis is focused on the pressure, given that from what has been observed, it is expected that its periodic fluctuations are the ones driving the fluctuations of the flow streamlines and therefore the shock oscillation itself.

Starting with Fig. 12, where the cross-correlation contour over the midpassage probe line is shown with the pressure signal at the top and the flow angle incidence at the bottom. The signals on the left side are bypass filtered between 500 and 700 Hz and on the right between 1100 and 1300 Hz. The pressure at these two frequency bands shows that most of the propagation occurring along the probe line is downstream. However, at higher frequencies, some upstream propagation occurs mostly after, but also before the shock at 34.8 m/s. A quick check through the data points confirms that this is approximately equal to the speed of sound subtracted by the mean flow velocity after the shock. The flow angle incidence also shows some upstream propagation, but only upstream of the shock. This supports earlier observations that in the sonic regime, the only mechanism of upstream propagation is through the oblique shocks that inevitably affect the inflow angle. Another point to note is how the pressure signal seems to change direction around 75% chord. This is a location that recurrently showed changes in propagation speed or direction.

However, one part that is not clear is at 500–700 Hz, where the pressure prior to the shock shows mostly downstream propagation, the incidence of the flow seems to have some upstream propagation in this same area. This upstream propagation could be attributed to the extending branches of the strong oblique shock that drives the main shock forward at this frequency, but may not cause a much higher increase in pressure than already done by the entire movement of the shock structure. Again, an analysis in a reference frame following the shock movement might be able to clarify these details. Higher frequency bands are not shown, but most of them seem to share similar interpretations as the 1100–1300 Hz band. Lastly, some of the decorrelations prior to 20% occur due to the probe line crossing the bow and lip shocks.

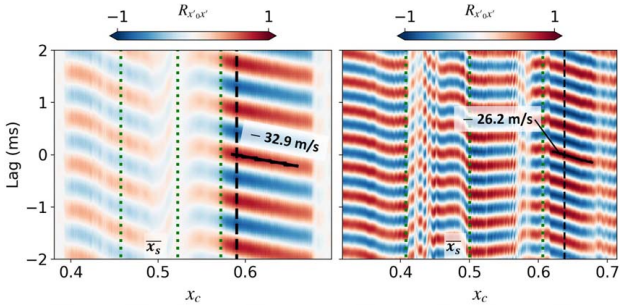

Fig. 11 Two-point cross-correlation contours along horizontal rows of the shadowgraph (left) and density gradient from simulations (right)

A similar analysis is shown in Fig. 13 for a line probe with a constant delta from the blade surface of 0.8 times the δ_{99} prior to the shock. This figure is organized the same way as Fig. 12, but is filtered between 1700 and 1900 Hz instead of 1100 and 1300 Hz. These graphs show that most of the pressure propagation after the shock is downstream. This was unexpected and rules out that the pressure waves observed in the passage also propagate somewhat in the blocks of separated flow convecting downstream. The flow incidence on the other hand is much more noisy after the shock, but prior to it, it clearly shows that the propagating pressure is accompanied by a flow angle variation. The 1100–1300 Hz band is not shown this time given that the signal does not have these clear trends. This is supported by the PSDs previously shown, as the interaction of the shock one way or another seems to shift the power in the spectra to those higher tones.

With the context provided from the previous analyses, the SPOD of the pressure field is now shown in Fig. 14. The SPOD evaluation followed the implementation of the algorithm by Schmidt et al. [31,32] in the python package from Ref. [33]. The dataset of 2016 snapshots is divided into seven blocks, overlapping by 50%. The Hamming window is used for the evaluation of the Fourier transform over each block, resulting in frequency bins of approximately 200 Hz. This helps leverage the amount of data available to obtain the most accurate solution, while maintaining the tonal information shown in Fig. 4.

The data are then analyzed one frequency at a time, first by constructing the snapshot matrix, $\hat{Q}$. This matrix has a shape $M \times N$

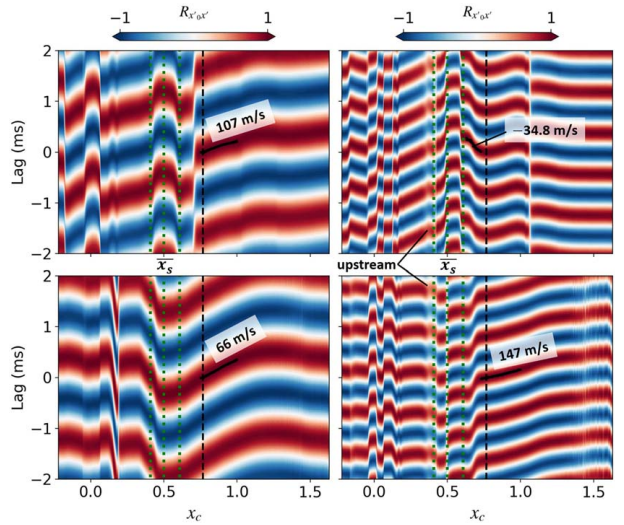

Fig. 12 Two-point cross-correlation along midpassage of the pressure (top) and flow incidence (bottom). Bypass filter applied between 500–700 Hz (left) and 1100–1300 Hz (right). Reference position marked with black dashed line.

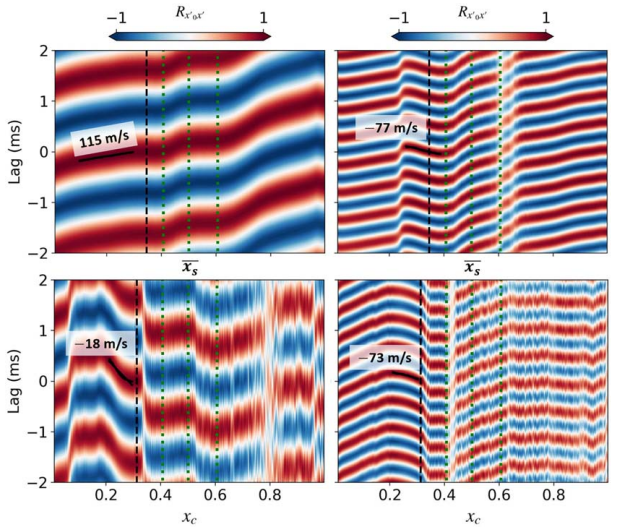

Fig. 13 Two-point cross-correlation along $0.8\delta_{99}$ of the pressure (top) and flow incidence (bottom). Bypass filter applied between 500–700 Hz (left) and 1700–1900 Hz (right). Reference position marked with black dashed line.

referring to the total number of degrees-of-freedom and realizations. Finally, the covariance matrix, $\hat{C}$, is calculated and used to solve the eigenvalue problem as follows:

$$\hat{C} = \frac{1}{N-1}\hat{Q}\hat{Q}^H \tag{2}$$

$$\hat{C}W\hat{\Phi} = \hat{\Phi}\hat{\Lambda} \tag{3}$$

where the superscript H refers to the Hermitian, $W = I$ is the so-called variance norm weighting for a regular grid of sampled values, and $\hat{\Phi}$ contains the eigenvectors of interest. The analysis shown in Fig. 14 focuses on the first modes, as they were observed to dominate the other ones considerably. The results are complemented by the SPOD of the velocity components performed in Parts I and II of this contribution. For further details on the implementations of this technique, the reader is referred to the respective papers and to the original material previously cited.

The results show an extension of what has been discussed thus far in this paper, even if modal analyses tend to become rather abstract and difficult to interpret at higher frequencies. Starting with the 600 Hz contour, the contour strongly marks the region where the shock is moving. This region is almost extended downstream in the area marked by the periodical flow separation due to the breakdown in the passage. It is also worth noting that the area around the trailing edge at these frequencies is in opposite phase. This supports the discussion from Sec. 5.1 on the effect of the vortex shedding at the trailing edge. We think the way and lag at which this interaction occurs is a key factor on the frequency of the main shock movement, but not necessarily the driving force behind it.

To look for this origin, the mode contour at 1200 Hz is presented, which strongly highlights an area around 70–90% chord length. This would match the region with evidence of upstream propagation of the pressure signal from previous discussions. This area extends across the passage and, along with the third frequency mode contour, seems to indicate that the pressure is fluctuating at these higher frequencies across the passage in a banded pattern due to the shocklets. We think this is a distinguishing feature of this mechanism of oscillation.

Lee's feedback mechanism points to the interactions of the flow with the trailing edge geometry as the origin of the disturbances that propagate upstream toward the shock and provoke its oscillation. However, it would be expected that such a mechanism would

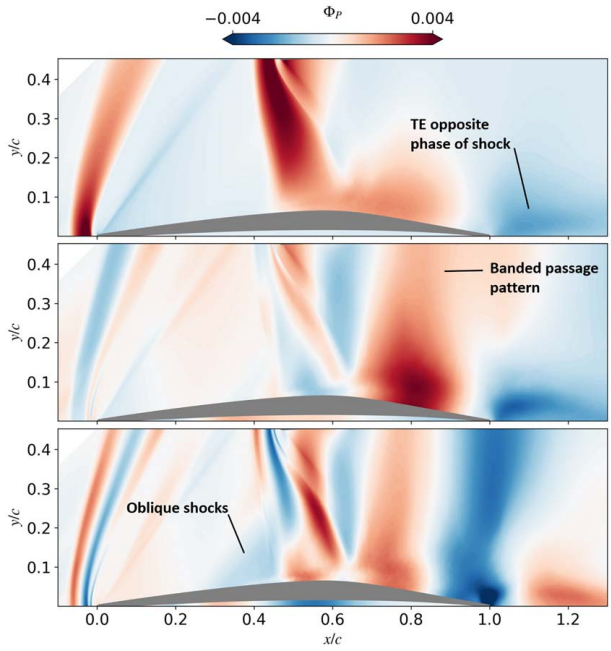

Fig. 14 First SPOD mode of the pressure field for the TCTA at 600, 1200, and 1800 Hz (top to bottom)

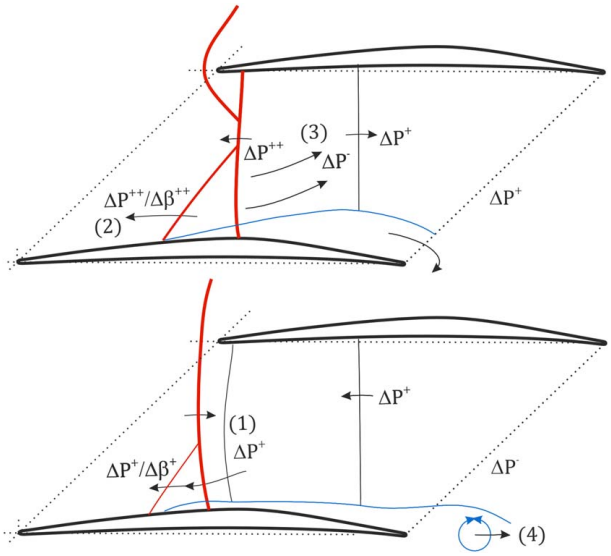

Fig. 15 Schematic of main mechanisms of shock oscillation responsible for upstream (top) and downstream (bottom) shock movement

propagate radially from an area resembling a point source. Instead, the evidence suggests that the disturbances originate upstream of the trailing edge. Even though they do not necessarily propagate along the suction surface, the separated flow is after all highly turbulent and convecting downstream, and they do propagate in the passage to interact strongly with the shock. This would be consistent with previous experimental HSPIV results of the LHT cascade, where disturbances were also reported to propagate from a point prior to the trailing edge. This is not to say that the trailing edge is not an important feature of the flow through the cascade. On the contrary, it seems to affect the frequency at which the entire oscillation plays out and is also observed to change the mode contour and concentrate a lot of energy. However, this mechanism seems to be a reaction to the complex interaction of the features converging in the passage when the shock is present.

Finally, the third frequency contour again presents the strongest indication of the oblique shocks occurring upstream of the shock. Interestingly, this is also the mode that concentrates the most energy at the trailing edge. Even if its transmission along the blade surface does not seem to show up in the cross-correlation plot of Fig. 13, it seems to be propagating nevertheless across the passage and to have more success upstream of the shock.

5.4 The Mechanisms of Shock Oscillation. In this section, we attempt to summarize the different observations and conclusions drawn from the previous analyses into a discrete number of aerodynamic mechanisms that visualize the current understanding of the oscillation in the passage of the TCTA. These mechanisms are then compared with what has been previously observed in earlier experiments in order to find points of commonality or divergence.

The flow in the cascade seems to be dominated by at least two main aerodynamic mechanisms, as illustrated in Fig. 15, which will be continuously referenced throughout this section. Within these mechanisms, there are a number of interactions or features that are not understood yet, but do not undermine the observations made so far. The first one is a mechanism of upstream propagation of pressure information in the passage of the cascade that occurs at high frequencies and continuously throughout the cycle. The origin of these disturbances seems to occur within a region inside the passage and before the trailing edge of the profile. This behavior is probably influenced by the properties of the turbulent flow downstream of the shock and how it interacts with the rest of the flow in the passage and the geometry itself. Given this, it seems to develop into planar waves of upstream pressure variations that were observed both in LES and experiments.

When these shocklets propagate upstream and reach the main shock, as shown at the bottom of Fig. 15, the pressure variations stop propagating due to the sonic flow upstream. However, the fluctuations do propagate through the subsonic part of the boundary layer and mostly at high-frequency tones. This transmission is not well understood and could hint either to non-linear interactions with the main shock or a physical mechanism of transmission along the shock as the shocklet arrives. What occurs upstream of the shock on the other hand is a lot more clear. The laminar boundary layer is weak and regular, allowing an easy propagation of these disturbances and causing it to separate and generate oblique shocks. These periodic high-frequency weak oblique shocks (1) are able to transmit these pressure fluctuations further upstream, but they also inevitably produce small changes in the flow angle and cause small high-frequency oscillations of the shock position itself, as described by Hergt et al. [19].

When these shocklets coincide with the main shock in the passage, they seem to trigger a major collapse of the flow due to decreased inflow angle, the oblique topology of the main shock, and the system of secondary shocks generated. The latter being exacerbated by the high-speed flow maintained in the passage and the coalescing shocklets. This seems to point to at least a momentary, but violent choking of the cascade, which creates a strong pressure buildup and culminates in a strong oblique shock propagating upstream at high speed (2). This oblique shock increases the flow angle immediately upstream of the main shock, which rapidly recovers a normal shock topology as it moves out of the passage. The oblique shock then also reaches the leading edge of the adjacent blade and directly influences the inflow angle and therefore the operating point of the entire periodic domain.

This leads to a second mechanism of downstream propagation that may be more directly responsible for the actual frequency of oscillation of the main shock. Given that there is a lag between the events in this cycle, the sudden increase in inflow angle is not accompanied by a stable pressure increase at the cascade outlet. Instead, the separated flow convecting downstream maintains regions of high-speed flow due to the blockage created in the passage (3). It also contains a lot of vortical structures that strongly interact with the trailing edge and create a temporary vortex

shedding that also decreases the back-pressure (4). The ingredients are then present for the shock to overshoot its upstream movement and compensate by moving into the passage again.

5.4.1 Parallels With Previous Experiments. Based on the previous discussion, it can be assumed that such mechanisms could only be present in cascade designs with sufficiently low stagger angle and Mach number. This so that the shock impinges at a location that allows considerable interactions of the wake with the throat and the rest of the passage. This is reminiscent of the author's recent experience with the TCTA in off-design point (ODP) conditions [20], and also of the LHT cascade [18,19], and the TFAST cascade also tested at the TGK [1,34]. Only HSS and snapshot PIV data are available for the latter, but the operating conditions are relevant and provide a good comparison, as measurements were also made with a turbulent boundary layer.

One last figure is then presented where the PSD of the shock motion recorded in these experiments is recalled, but this time recasted in a frequency-weighted spectra form, as shown in Fig. 16. This form helps identify, as was done for the TCTA, that the main movement of the shock is occurring at the lower broad frequency bands peaking at 510, 180, 207, and 360 Hz for the TCTA-ADP, TCTA-ODP, LHT, and TFAST cascades, respectively. Most of the time, this main oscillation is modulated by high-frequency tones. The only exception is the spectra of the TFAST cascade with the tripped boundary layer. This is an interesting behavior that has also been observed in other studies with high-fidelity numerical methods [14].

This behavior is also consistent with the mechanisms described in this section. Indeed, we have provided a physical reasoning for the tones observed in the spectra from the upstream propagation of periodic pressure fluctuations that turn into oblique shockwaves in the laminar flow region upstream of the shock. A turbulent boundary layer upstream of the shock would not only be much more robust to this separation but would also transmit these weaker high-frequency pressure variations in a more noisy and uneven pattern. This would naturally prevent an extended separation of the upstream boundary layer and therefore of the high-frequency modulation of the shock position.

Another interesting observation is how the TFAST and TCTA cascades at ODP and ADP have almost identical high-frequency tones. Even though this might suggest at first that there is some effect of the wind tunnel coming into play or helping amplify this specific frequency, it must be noted that the two cascade designs have the same chord size and comparable pitches and stagger angles. The tone on the other hand is strongly shifted for the LHT cascade, which differs a lot more in terms of these features. This might suggest that the higher frequencies could be heavily influenced by the geometrical features and design of the cascade itself, and less so of the profile.

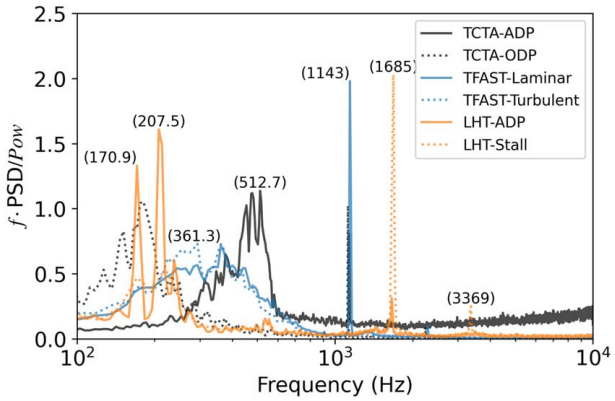

Fig. 16 Frequency-weighted PSD of shock oscillation for different experiments at the DLR's TGK

Table 2 Dimensional analysis of shock oscillation frequencies

		TCTA-ADP	TCTA-ODP	LHT	TFAST
Low-freqs.					
	St_c	0.137	0.0561	0.0441	0.0970
	$St_{\delta_{99}}$	0.00058	–	0.00019	–
	St_1	0.202	0.111	0.0607	0.230
	St_2	0.277	0.116	0.0703	0.287
	St_3	0.352	0.209	0.108	0.495
High-freqs.					
	St_c	0.307	0.339	0.358	0.306
	$St_{\delta_{99}}$	0.0013	–	0.0015	–
	St_1	0.450	0.669	0.492	0.726
	St_2	0.618	0.701	0.571	0.906
	St_3	0.786	1.26	0.872	1.56

As a final comparison, Table 2 is presented, where the knowledge gathered is used to search for the best set of dimensional factors that may collapse either the low-frequency bands or the high-frequency tones in Fig. 16. For this purpose, the information compiled in Table 1 is used to come up with what the authors hope will be a growing compilation of data with the purpose of searching the main factors influencing the frequencies observed. The velocity of the flow before and after the shock has been estimated from the averaged PIV velocity fields available from the different tests. This was done by averaging the velocity along rows and columns in the area before (or after) the shock, away from the boundary layer, and within the field of view available.

The frequencies are first compared in terms of the classical definitions of the Strouhal number (St), based on the convective units ($\mathrm{St}_c = f \cdot c/V_1$) and on the boundary layer size and velocity prior to the shock ($\mathrm{St}_{\delta_{99}} = f \cdot \delta_{99}/V_{s_1}$). The formulations 1–3 are some of the ones attempted based on the factors observed to be playing a role at the different frequencies studied. The first two are $\mathrm{St}_1 = f \cdot c_a/(s_{s_2} - V_{s_2})$ and $\mathrm{St}_2 = f \cdot t/(s_{s_2} - V_{s_2})$. Here, c_a is the distance between the mean shock position and the trailing edge in the chord axis, or also the area where disturbances in the passage might occur. Furthermore, s_{s_2} is an estimate of the average speed of sound after the shock.

The third formulation is inspired by the acoustic feedback-type mechanism formulations presented by Rossiter in Ref. [35] and also applied in Ref. [14]:

$$\mathrm{St}_3 = f \cdot \left(\frac{c_b}{0.8 V_{s_2}} + \frac{c_b}{s_{s_2} - V_{s_2}} \right) \tag{4}$$

where c_b is the distance between the mean shock position and the 80% chord point along the chord axis, which seemed to be the point of origin of the disturbances. The term $0.8V_{s_2}$ on the other hand estimates the convection speed of the large eddies after the shock. In general, after trying different combinations observed in the literature as well, we found no special combination that would collapse this dataset. The high-frequency tones are the ones that lie the closest to each other, and the objective then lies on finding the factors that link the LHT cascade with the rest of the dataset. Using the geometrical features of the cascade for instance seems to help collapse the TCTA and the LHT data, but does not work as well with the TFAST cascade. The lower frequency bands seem to be even harder to compare than the tones.

In Part II of this series, it was noted that the laminar separation bubble length taken from the averaged velocity field of the LES provided a Strouhal number in the same order of magnitude as the 0.03 number reported for canonical oblique shock SBLIs [10,36]. However, this comparison is difficult to make with the experimental data given that the PIV measurements are rarely able to properly capture the full extent of the boundary layer separation. This is especially the case for the higher Mach number cases, where the flow exhibits several periods of open separation behind the shock. A

rough estimate of the separation length could be provided in future analyses based on the contours of the PIV windows available, but it would carry considerable uncertainty.

Nevertheless, this is just a beginning toward understanding these measurements as a whole. Some of the missing data could be estimated in the future. However, the objective is rather to focus future projects, or possibly influence other researchers, toward gathering data on these features that seem to be playing a role in the oscillation of the shock.

5.4.2 From Inertial to Rotating Frames of Reference. The ability to identify and classify the mechanisms described has been facilitated in this study by the use of a 2D geometry in an inertial reference frame. However, real applications would involve 3D designs and operating conditions that are inevitably affected by the forces generated in non-inertial frames of reference and the secondary flow effects near the blade tip. Even though it is not trivial to extrapolate the mechanisms presented, it can be generally assumed that if the given blade section has similar geometrical and inflow properties as the one studied in this paper, then a similar type of shock oscillation spectra could be possible. Most probably, however, with increasingly shifted peaks of oscillation depending on the severity of the additional effects.

This assumption is based on the experience gathered here by comparing experimental and LES results. For instance, it was observed that the spectrum was spread into a more broadband oscillation with a lower frequency peak probably due to the finite stiffness of the blade and the effects of the 3D shock front. These effects would be intensified when, for example, the separated boundary layer flow no longer convects mostly downstream to interact with the passage and the trailing edge, but also radially. Another expected difference would be a lower severity of the shock oscillation with respect to the one observed in the linear cascade case. This is based on the LES results showing a more severe shock oscillation than the experiments. The effect was understood to be probably caused by the perfectly periodic and generally 2D shock front obtained in the LES when compared to the flow in the test section.

A better understanding of the differences would inevitably require a methodical study transitioning from inertial to non-inertial frame of reference with a known baseline geometry. Nevertheless, the mechanisms explained are general enough to have possible applicability to more realistic operating conditions, even if they would inevitably become more complex and distorted than the ones presented in this paper.

6 Conclusions and Perspectives

The comparison of experimental and numerical data is never a trivial task, especially when dealing with such complex phenomena such as the SBLI inside of a transonic compressor cascade. Nevertheless, in this three-part series, we have brought together state-of-the-art numerical and experimental techniques to not only bring new knowledge in their respective fields, but also to gain an improved understanding on where they differ and why. This process enhanced the conclusions made at each step with respect to those that would have been gathered if performed separately as isolated work packages.

After describing the experimental methods that allowed the detailed analysis of the SBLI in Part I, and performing a thorough comparison of the numerical methods that allowed the same analysis numerically in Part II, this paper has brought their main results together for deeper analysis. By doing this, some possible answers were provided to the complex questions posed at the beginning regarding the high-frequency tones and low-frequency band of the shock oscillation observed within the TCTA cascade: Both frequencies are linked to the generation and propagation of disturbances upstream of the trailing edge driven by the interaction of separated flow structures with the flow in the passage; these disturbances propagate acoustically in the subsonic regime and continue in the sonic regime in the form of oblique shocks that also inevitably affect the operating point of the cascade; lastly, the high-frequency tones are related to mechanisms of upstream propagation of these disturbances facilitated by the laminar boundary layer, while the main shock movement is related to periodic interactions between these features culminating in stronger fluctuations of the operating point.

This paper not only explained the current understanding of these mechanisms but also highlighted the different aspects that are simply not understood yet. This includes, for example, the transmission of the shocklets into higher frequency fluctuations upstream of the shock. By identifying and separating these unknowns, we hope to prepare them for further analysis and discussion in future studies. As more high-quality experimental and numerical data are gathered, the need grows to categorize them and to search a global understanding that joins them together into an eventual global theory of SBLI in compressor cascades. This effort will require the contribution of numerous disciplines and stakeholders, as well as the further integration of experimental and numerical methods in the search for answers.

Acknowledgment

The authors would like to express their gratitude to Jasmin Flamm, Sebastian Grund, and the dedicated team of technicians operating the Transonic Cascade Wind Tunnel for their invaluable contributions. We also extend our appreciation to Dr. Romain Gojon for his insightful discussions during the data analysis phase.

Funding Data

- European Union's Horizon 2020 Research and Innovation Program (EC Grant 860909).
- High Performance Computing Center Stuttgart (Grant TCTA-SBLI/44238).

Conflict of Interest

There are no conflicts of interest.

Data Availability Statement

The datasets generated and supporting the findings of this article are obtainable from the corresponding author upon reasonable request.

Nomenclature

c = blade chord (mm)
s = speed of sound (m/s)
t = cascade pitch (mm)
M = Mach number
P = pressure (Pa)
T = temperature (K)
V = velocity (m/s)
t_c = convective time units $= cu_1^{-1}$ (s)
x_s = shock position (mm)
$R_{x_0'x'}$ = cross-correlation coefficient
δ_{99} = boundary layer height (mm)
u, v = velocity components along x, y (m/s)
AVDR = axial velocity density ratio $= \rho_2 V_2 \sin\beta_2 / \rho_1 V_1 \sin\beta_1$
DH = de Haller number
FT = flow turning $= \beta_1 - \beta_2$ (deg)
Pow = power (W)
St = Strouhal number

Greek Symbols

β = flow or geometry angle (deg)
ξ, η, ζ = streamwise, wall-normal, spanwise coordinates

Superscripts and Subscripts

1 = value at inlet
2 = value at outlet
s_1 = value upstream of shock
s_2 = value downstream of shock

Acronyms

ADP = aerodynamic design point
DGSEM = discontinuous Galerkin spectral element method
HSS = high-speed Schlieren
LES = large eddy simulation
MP = measurement plane
ODP = off-design point
PIV = particle image velocimetry
PSD = power spectral density
SBLI = shock-boundary layer interaction
SPOD = spectral proper orthogonal decomposition
TCTA = Transonic Cascade TEAMAero
TGK = Transonic Cascade Wind Tunnel

References

[1] Hergt, A., Klinner, J., Wellner, J., Willert, C., Grund, S., Steinert, W., and Beversdorff, M., 2019, "The Present Challenge of Transonic Compressor Blade Design," ASME J. Turbomach., **141**(9), p. 091004.

[2] Epstein, A. H., Kerrebrock, J. L., and Thompkins, W. T., 1979, "Shock Structure in Transonic Compressor Rotors," AIAA J., **17**(4), pp. 375–379.

[3] Ferri, A., 1939, "Investigations and Experiments in the Guidonia Wind Tunnel," 12-15Hauptversammlung der Lilienthal-Gesellschaft für Luftfahrtforschung, Oct. 12–15, National Advisory Committee for Aeronautics, Berlin, pp. 1–33.

[4] Fage, A., and Sargent, R. F., 1947, "Shock-Wave and Boundary-Layer Phenomena Near a Flat Surface," Proc. R. Soc. Lond. A., **190**(1020), pp. 1–20.

[5] Dupont, P., Piponniau, S., Sidorenko, A., and Debiève, J. F., 2008, "Investigation by Particle Image Velocimetry Measurements of Oblique Shock Reflection With Separation," AIAA J., **46**(6), pp. 1365–1370.

[6] Lee, B. H., 1990, "Oscillatory Shock Motion Caused by Transonic Shock Boundary-Layer Interaction," AIAA J., **28**(5), pp. 942–944.

[7] Crouch, J. D., Garbaruk, A., Magidov, D., and Travin, A., 2009, "Origin of Transonic Buffet on Aerofoils," J. Fluid Mech., **628**, pp. 357–369.

[8] Pirozzoli, S., Grasso, F., and Gatski, T. B., 2005, "DNS Analysis of Shock Wave/Turbulent Boundary Layer Interaction at $M = 2.25$," 4th International Symposium on Turbulence and Shear Flow Phenomena, Williamsburg, VA, June 26–29.

[9] Dussauge, J. P., and Piponniau, S., 2008, "Shock/Boundary-Layer Interactions: Possible Sources of Unsteadiness," J. Fluids Struct., **24**(8), pp. 1166–1175.

[10] Touber, E., and Sandham, N. D., 2009, "Large-Eddy Simulation of Low-Frequency Unsteadiness in a Turbulent Shock-Induced Separation Bubble," Theor. Comput. Fluid Dyn., **23**(2), pp. 79–107.

[11] Lee, B. H., 2001, "Self-sustained Shock Oscillations on Airfoils at Transonic Speeds," Prog. Aerosp. Sci., **37**(2), pp. 147–196.

[12] Hartmann, A., Feldhusen, A., and Schröder, W., 2013, "On the Interaction of Shock Waves and Sound Waves in Transonic Buffet Flow," Phys. Fluids, **25**(2), p. 026101.

[13] Garnier, E., and Deck, S., 2010, "Large-Eddy Simulation of Transonic Buffet Over a Supercritical Airfoil," Turbulence and Interactions 2009, La Martinique, France, May 31–June 5.

[14] Priebe, S., Wilkin II, D., Breeze-Stringfellow, A., Mousavi, A., and Bhaskaran, R., 2022, "Large Eddy Simulations of a Transonic Airfoil Cascade," ASME Turbo Expo 2022, Rotterdam, the Netherlands, June 13–17.

[15] Ranjan Majhi, J., and Venkatraman, K., 2023, "On the Nature of Transonic Shock Buffet in an Axial-Flow Fan," AIAA J., **61**(12), pp. 5390–5403.

[16] Schreiber, H.-A., 1976, *Investigation of Two Transonic Compressor Cascades and Comparison With Rotor Data*, Deutsches Zentrum für Luft- und Raumfahrt, Cologne.

[17] Schreiber, H.-A., and Starken, H., 1981, "Evaluation of Blade Element Performance of Compressor Rotor Blade Cascades in Transonic and Low Supersonic Flow Range," International Symposium on Air Breathing Engines, 5th, Bangalore, India, Feb. 16–22, pp. 61–67.

[18] Klinner, J., Hergt, A., Grund, S., and Willert, C. E., 2021, "High-Speed PIV of Shock Boundary Layer Interactions in the Transonic Buffet Flow of a Compressor Cascade," Exp. Fluids, **62**(3), pp. 1–9.

[19] Hergt, A., Klinner, J., Willert, C., Grund, S., and Steinert, W., 2022, "Insights Into the Unsteady Shock Boundary Layer Interaction," ASME Turbo Expo 2022, Rotterdam, The Netherlands, June 13–17.

[20] Munoz Lopez, E., Hergt, A., Klinner, J., Grund, S., Flamm, J., and Gümmer, V., 2023, "Investigations of the Unsteady Shock-Boundary Layer in a Transonic Compressor Cascade," ASME Turbo Expo 2023, Boston, MA, June 26–30.

[21] Klinner, J., Munoz Lopez, E. J., Hergt, A., and Willert, C., 2023, "High-Resolution PIV Measurements of the Shock Boundary Layer Interaction Within a Highly Loaded Transonic Compressor Cascade," International Symposium on Particle Image Velocimetry 2023, San Diego, CA, June 19–21.

[22] Morsbach, C., Bergmann, M., Tosun, A., Klose, B. F., Bechlars, P., and Kügeler, E., 2024, "A Numerical Test Rig for Turbomachinery Flows Based on Large Eddy Simulations With a High-Order Discontinuous Galerkin Scheme—Part 3: Secondary Flow Effects," ASME J. Turbomach., **146**(2), p. 021007.

[23] Bergmann, M., Morsbach, C., Klose, B. F., Ashcroft, G., and Kügeler, E., 2024, "A Numerical Test Rig for Turbomachinery Flows Based on Large Eddy Simulations With a High-Order Discontinuous Galerkin Scheme—Part I: Sliding Interfaces and Unsteady Row Interactions," ASME J. Turbomach., **146**(2), p. 021007.

[24] Klose, B. F., Morsbach, C., Bergmann, M., Hergt, A., Klinner, J., Grund, S., and Kügeler, E., 2024, "A Numerical Test Rig for Turbomachinery Flows Based on Large Eddy Simulations With a High-Order Discontinuous Galerkin Scheme—Part II: Shock Capturing and Transonic Flows," ASME J. Turbomach., **146**(2), p. 021007.

[25] Klose, B. F., Munoz Lopez, E. J., Hergt, A., Klinner, J., Bergmann, M., and Morsbach, C., 2024, "Analysis of a Transonic Cascade With Wall-Modeled LES Based on DGSEM," *Direct and Large Eddy Simulation XIII*, C. Marchioli, M V. Salvetti, M. Garcia-Villalba, and P. Schlatter, eds., Springer Nature, Switzerland, pp. 157–163.

[26] Hergt, A., Klose, B., Klinner, J., Bergmann, M., Munoz Lopez, E. J., Grund, S., and Morsbach, C., 2023, "On the Shock Boundary Layer Interaction in Transonic Compressor Blading," ASME Turbo Expo 2023, Boston, MA, June 26–30.

[27] Munoz Lopez, E. J., Hergt, A., Grund, S., and Gümmer, V., 2023, "The New Chapter of Transonic Compressor Cascade Design at the DLR," ASME J. Turbomach., **145**(8), p. 081001.

[28] Munoz Lopez, E. J., Hergt, A., Ockenfels, T., Grund, S., and Gümmer, V., 2023, "The Current Gap Between Design Optimization and Experiments for Transonic Compressor Blades," Int. J. Turbomach. Propul. Power, **8**(4), p. 47.

[29] Schlüß, D., Frey, C., and Ashcroft, G., 2016, "Consistent Non-reflecting Boundary Conditions for Both Steady and Unsteady Flow Simulations in Turbomachinery Applications," 7th European Congress on Computational Methods in Applied Sciences and Engineering (ECCOMAS), Hersonissos, Greece, June 5–10.

[30] Pirozzoli, S., 2011, "Numerical Methods for High-Speed Flows," Annu. Rev. Fluid Mech., **43**(1), pp. 163–194.

[31] Towne, A., Schmidt, O. T., and Colonius, T., 2018, "Spectral Proper Orthogonal Decomposition and Its Relationship to Dynamic Mode Decomposition and Resolvent Analysis," J. Fluid Mech., **847**, pp. 821–867.

[32] Schmidt, O. T., and Colonius, T., 2020, "Guide to Spectral Proper Orthogonal Decomposition," AIAA J., **58**(3), pp. 1023–1033.

[33] Mengaldo, G., and Maulik, R., 2021, "PySPOD: A Python Package for Spectral Proper Orthogonal Decomposition (SPOD)," J. Open Sourc. Softw., **6**(60), p. 2862.

[34] Klinner, J., Hergt, A., Grund, S., and Willert, C. E., 2019, "Experimental Investigation of Shock-Induced Separation and Flow Control in a Transonic Compressor Cascade," Exp. Fluids, **60**, Article Number 96.

[35] Rossiter, J. E., 1964, "Wind-Tunnel Experiments on the Flow Over Rectangular Cavities at Subsonic and Transonic Speeds," ARC 26621, Ministry of Aviation.

[36] Bergier, T., Gojon, R., Fiore, M., Gressier, J., Jamme, S., and Joly, L., 2023, "Sweep Effects on a Canonical Shock Wave/Boundary Layer Interaction," Int. J. Heat Fluid Flow, **104**, p. 109227.